Lagrangian investigations on velocity gradients in compressible turbulence: Examination of viscous process and flow-field topology

Nishant Parashar[1]†, Sawan Suman Sinha [1] and Balaji Srinivasan[2]

[1]Department of Applied Mechanics, Indian Institute of Technology Delhi, New Delhi 110016, India

[2]Department of Mechanical Engineering, Indian Institute of Technology Madras, Chennai 600036, India

(Received xx; revised xx; accepted xx)

We perform Lagrangian investigations (following fluid particles) of the dynamics of velocity gradients in compressible decaying turbulence. Specifically, we examine (i) the evolution of the viscous process in the governing equation of the velocity gradient tensor, and (ii) evolution of the invariants of the velocity gradient tensor. Well-resolved direct numerical simulations over a range of Mach and Reynolds number along with a Lagrangian particle tracker are employed for our investigations. We find that an increase in the initial turbulent Mach number tends to intensify the viscous process following fluid particles. We provide evidence and explain that this intensification is attributable to the development of a large disparity in the magnitude of the velocity gradients associated with contracting and expanding fluid particles combined with the overall preferences of the these contracting and expanding fluid particles to change their dilatation rate. Further, we examine the performance of the so-called *linear Lagrangian diffusion model* (LLDM) of the viscous process. Subsequent to identifying the shortcomings of the model, we propose some suggestions for model improvement as well. In the second part of the study, we employ our DNS results to examine the trajectories of fluid particles in the the space of the invariants of the velocity gradient tensor. Such an examination allows us to accurately measure the lifetimes of major topologies of compressible turbulence and provide explanation why some selective topologies tend to exit longer than the others.

1. Introduction

Gradients of the small-scale velocity field and its dynamics in a turbulent flow influence many important nonlinear turbulence processes like cascade, mixing, intermittency and material element deformation. Thus, examination of the velocity gradient tensor in canonical turbulent flow fields have been the subject of interest employing experimental measurements (Lüthi *et al.* 2005), direct numerical simulations (DNS) (Ashurst *et al.* 1987*b*), as well as simple autonomous dynamical models (ordinary differential equations) (Vieillefosse 1982; Cantwell 1992) of velocity gradients. The pioneering work done by the cited authors have been further followed up extensively by several researchers for both incompressible (Ashurst *et al.* 1987*b*,*a*; Girimaji 1991; Ohkitani 1993; Pumir 1994; Girimaji & Speziale 1995; O'Neill & Soria 2005; Chevillard & Meneveau 2006; da Silva & Pereira 2008; Chevillard & Meneveau 2011) and compressible turbulence (Soria *et al.*

† Email address for correspondence: nishantparashar14@gmail.com

1994; Pirozzoli & Grasso 2004; Suman & Girimaji 2009, 2010, 2012; Wang & Lu 2012; Vaghefi & Madnia 2015; Danish *et al.* 2016*a*; Parashar *et al.* 2017*a*). These efforts have led to an improved understanding of small-scale turbulence.

Most DNS or experiment-based studies of fluid mechanics have so far been performed using the Eulerian approach. However, it is desirable to investigate various flow physics following individual fluid particles (the Lagrangian tracking) as well. Such an investigation is especially required from the point of view of developing/improving simple dynamical models of the velocity gradients like the restricted Euler equation (REE) (Cantwell 1992; Girimaji & Speziale 1995; Meneveau 2011) and the enhanced homogenized Euler equation model of Suman & Girimaji (2009). Such simple models, in turn, can be used for closure of Lagrangian PDF method of turbulence (Pope 2002). An apt example of how Lagrangian statistics can reveal more profound insights into velocity gradient dynamics is the recent experimental study of Xu *et al.* (2011), wherein the authors provided evidence of the so-called "Pirouette effect". Even though the vorticity vector had always been expected to align with the largest strain-rate eigenvector, Eulerian investigations invariably revealed a counterintuitive picture of vorticity aligning most strongly with the intermediate eigenvector of the instantaneous local strain-rate tensor. Xu *et al.* (2011), with their experimental Lagrangian investigations, provided first-hand evidence that indeed the vorticity vector dynamically attempts to align with the largest strain-rate eigenvector of an initial reference time in order to cause intense vortex stretching, and the alignment tendency as shown by the Eulerian one-time field (with the instantaneous intermediate eigenvector) was merely a transient and incidental picture.

In incompressible flows, Lagrangian studies using the direct numerical simulation of decaying turbulence have earlier been performed by Yeung & Pope (1989) and Girimaji & Pope (1990*b*). Yeung & Pope (1989) focused on Lagrangian statistics of velocity, acceleration, and dissipation. Girimaji & Pope (1990*b*) examined the evolution of material elements in incompressible decaying turbulence. Recently, Xu *et al.* (2011) have complemented their experimental observations of vorticity alignment with the Lagrangian data extracted from DNS of forced isotropic turbulence as well. Chevillard & Meneveau (2011) evaluated the Lagrangian model for velocity gradient tensor for its capability to predict vorticity alignment using Lagrangian data obtained from DNS of forced isotropic turbulent flow. Bhatnagar *et al.* (2016) quantified the persistence time of fluid particles in vorticity-dominated and strain-dominated topologies using Lagrangian data obtained from DNS of isotropic forced incompressible turbulence.

In compressible turbulence, Lagrangian statistics of velocity gradients have been recently studied by Danish *et al.* (2016*a*) and Parashar *et al.* (2017*a*). While Danish *et al.* (2016*a*) provided the first glimpse of compressibility effects on the alignment tendencies of the vorticity vector, Parashar *et al.* (2017*a*) followed it up and made attempts at explaining the observed behavior in terms of the dynamics of the inertia tensor of fluid particles and conservation of angular momentum of tetrads representing fluid particles. In continuation of our effort to develop deeper insight into the dynamics of small-scale turbulence from a Lagrangian perspective, in this work, we focus on another two important aspects of velocity gradient dynamics: (i) evolution of the viscous process and the role of the deformation gradient tensor in it, and (ii) dynamics of flow field topology in compressible turbulence.

Our primary motivation behind investigating the dynamics of the deformation gradient tensor is that this quantity has been used in modeling the viscous processes in restricted Euler equation (REE) by Jeong & Girimaji (2003). The authors modeled the viscous process using the gradient-diffusion hypothesis, wherein diffusion is allowed to

be amplified as a function of the deformation gradient tensor. This model was called the linear Lagrangian diffusion model (LLDM). Later the same model was used by Suman & Girimaji (2009) in their enhanced homogenized Euler equation (EHEE) model. Even though the EHEE model employing the LLDM approach does capture some Mach number and Prandtl number effects, further improvements are indeed desirable (Danish *et al.* 2014). From this point of view, in the first part of this work, we examine the influence of compressibility on the exact viscous process in the Lagrangian dynamics of velocity gradients, and subsequently subject the LLD modeling approach to a direct scrutiny by comparing its Lagrangian evolution history against that of the exact process it represents. Direct numerical simulation data of decaying compressible turbulence over a wide range of Mach number along with a well-validated Lagrangian particle tracker is employed for the purpose. The influence of compressibility on the exact viscous process is parameterized in terms of Mach number and dilatation rate.

In the second part of this work, we examine the evolution of flow-field topology in compressible turbulence following the Lagrangian trajectories (LT) of the invariants of the velocity gradient tensors. Topology can be visualized as the local streamline pattern, observed with respect to a reference frame which is translating with the center of mass of a local fluid particle (Chong *et al.* 1990). Topology actually depends on the nature of eigenvalues of the velocity gradient tensor (VGT), but can also be readily determined by knowing the three invariants of the VGT (Cantwell & Coles 1983; Chong *et al.* 1990). Flow field topology can also be used for visualization of a flow field. Further, topology has been shown to reveal deeper insights into various nonlinear turbulence processes as well (Cantwell 1993; Soria *et al.* 1994). Recently, Danish *et al.* (2016*b*) have also attempted developing models for scalar mixing using topology as a conditioning parameter.

Traditionally, due to the prohibitive demand of computational resources, dynamics of topology have been studied employing an approximate surrogate method called the conditional mean trajectory (CMT). The idea of CMT was proposed by Martín *et al.* (1998), who employed merely one-time velocity gradient data of the entire flow field and computed bin-averaged rates-of-change of second and third invariants of VGT using the right-hand-side of evolution equations of the invariants. These bin-averaged rates of change conditioned upon their locations were subsequently used to plot trajectories in the space of VGT invariants. The authors called these trajectories as conditional mean trajectories (CMT) and used them as a surrogate approach to study invariant dynamics. Subsequently, several authors have employed the CMTs to investigate various aspects of topology dynamics both for incompressible (Martín *et al.* 1998; Ooi *et al.* 1999; Elsinga & Marusic 2010; Meneveau 2011; Atkinson *et al.* 2012; Zhou *et al.* 2015) and compressible flows (Chu & Lu 2013; Bechlars & Sandberg 2017). Even though CMTs do provide some useful information about dynamics of invariants, they are after all an approximation and merely a surrogate approach in the absence of adequate computational resources (Martín *et al.* 1998). An investigation of the *exact* Lagrangian dynamics in compressible turbulence must be performed, if adequate computational resources are available. Indeed such an investigation of invariants using Lagrangian trajectories have been recently performed by Bhatnagar *et al.* (2016) for incompressible turbulence. Based on such a motivation, we employ the LTs to investigate lifetime of topologies and their interconversion processes in compressible turbulence.

To address the identified objectives of this paper, we employ direct numerical simulations of decaying isotropic compressible turbulence over a wide range of turbulent Mach number (0.075, 1.5) and a moderate range of Reynolds number (70, 350). The Lagrangian dynamics are obtained using an almost time continuous set of Eulerian flow fields along with spline-aided Lagrangian particle tracker (more details in §4).

This paper is organized into six sections. In §2 we present the governing equations. In §3 we provide details of our direct numerical simulations as well as the Lagrangian particle tracker. In §4 we examine the influence of compressibility on the viscous processes of the velocity gradient dynamics and evaluate the LLD model. In §5 we study the dynamics of topologies, compare CMT and LT and quantify lifetimes of various flow-topologies existing in compressible turbulence. Section 6 concludes the paper with a summary.

2. Governing Equations

The evolution of a compressible flow field is governed by the following equations:

$$\frac{\partial \rho}{\partial t} + V_k \frac{\partial \rho}{\partial x_k} = - \rho \frac{\partial V_k}{\partial x_k}; \tag{2.1}$$

$$\frac{\partial V_i}{\partial t} + V_k \frac{\partial V_i}{\partial x_k} = - \frac{1}{\rho}\frac{\partial p}{\partial x_i} + \frac{1}{\rho}\frac{\partial \sigma_{ik}}{\partial x_k}; \tag{2.2}$$

$$\begin{aligned} \frac{\partial T}{\partial t} + V_k \frac{\partial T}{\partial x_k} = & - T(n-1)\frac{\partial V_i}{\partial x_i} - \frac{n-1}{\rho R}\frac{\partial q_k}{\partial x_k} \\ & + \frac{n-1}{\rho R}\frac{\partial}{\partial x_j}\left(V_i \sigma_{ji}\right); \end{aligned} \tag{2.3}$$

$$p = \rho R T; \tag{2.4}$$

where V_i and x_i represents the velocity and position vector respectively. The thermodynamic properties are represented by ρ (density), p (pressure) and T (temperature), while R and n denotes the gas constant and specific heat ratio respectively. Equation (2.1) is the continuity equation, (2.2) represents the momentum conservation equations, (2.3) is the equation of energy conservation and (2.4) is the equation of state for a perfect gas. Heat flux (q_k) and the specific heat ratio (σ_{ij}) are found using the following constitutive relationships:

$$\sigma_{ij} = \mu\left(\frac{\partial V_i}{\partial x_j} + \frac{\partial V_j}{\partial x_i}\right) + \delta_{ij}\lambda\frac{\partial V_k}{\partial x_k}; \tag{2.5}$$

$$q_k = -K\frac{\partial T}{\partial x_k}; \tag{2.6}$$

where, K is the thermal conductivity, μ is the first coefficient of viscosity and λ denote the second coefficient of viscosity ($\lambda = -\frac{2\mu}{3}$). The velocity gradient tensor is defined as:

$$A_{ij} \equiv \frac{\partial V_i}{\partial x_j}.$$

By taking the gradient of momentum equation (2.2), the evolution equation of A_{ij} can be obtained:

$$\begin{aligned} \frac{DA_{ij}}{Dt} = & -A_{ik}A_{kj} - \underbrace{\frac{\partial}{\partial x_j}\left(\frac{1}{\rho}\frac{\partial p}{\partial x_i}\right)}_{\mathbb{P}_{ij}} \\ & + \underbrace{\frac{\partial}{\partial x_j}\left\{\frac{1}{\rho}\frac{\partial}{\partial x_k}\left[\mu\left(\frac{\partial V_i}{\partial x_k} + \frac{\partial V_k}{\partial x_i} - \frac{2}{3}\frac{\partial V_p}{\partial x_p}\delta_{ik}\right)\right]\right\}}_{\Upsilon_{ij}}; \end{aligned} \tag{2.7}$$

where, $\mathbb{P}_{ij}$ is the pressure Hessian tensor and Υ_{ij} is the viscous process governing the evolution of the velocity gradient tensor. The rate of change following a fluid particle

is caculated using the substantial derivative, which is represented by the operator $\frac{D}{Dt}(\equiv \frac{\partial}{\partial t} + V_k \frac{\partial}{\partial x_k})$.

3. Direct numerical simulations and particle tracking

Our direct numerical simulations of nearly incompressible and compressible decaying turbulence are performed using the gas kinetic method (GKM). GKM was originally developed by Xu (2001) and has been shown to be quite robust in terms of numerical stability. Further, GKM has the ability to capture shocks without producing numerical oscillations. Several researchers have employed GKM for simulating compressible decaying turbulence (Kerimo & Girimaji 2007; Liao *et al.* 2009; Kumar *et al.* 2013; Parashar *et al.* 2017*b*).

Our computational domain is of size 2π with a uniform grid and periodic boundary conditions imposed on opposite sides of the domain. The initial velocity field is generated at random with zero mean and having the following energy spectrum $E(\kappa)$:

$$E(\kappa) = A_0 \kappa^4 \exp\left(-2\kappa^2/\kappa_0^2\right), \tag{3.1}$$

where κ is wavenumber. Values for spectrum constants A_0 and κ_0 are provided in Table 1 for various simulations employed in this work. The relevant Reynolds number for isotropic turbulence is the one based on Taylor micro-scale (Re_λ):

$$Re_\lambda = \sqrt{\frac{20}{3\epsilon\nu}} k, \tag{3.2}$$

where k, ϵ, and ν represent turbulent kinetic energy, its dissipation-rate, and kinematic viscosity. For compressible isotropic turbulence, the relevant Mach number is the turbulent Mach number (M_t):

$$M_t = \sqrt{\frac{2k}{nR\overline{T}}}, \tag{3.3}$$

where $\overline{T}$ represents mean temperature.

Following the work of Kumar *et al.* (2013), we have used a 4^{th} order accurate weighted-essentially-non-oscillatory (WENO) method for interpolation of flow variables. Our solver has been extensively validated with established DNS results of compressible turbulent flows (Danish *et al.* 2016*a*). In total, this study employs seven different simulations (Simulations A-G). Descriptions of these simulations are presented in Table 1.

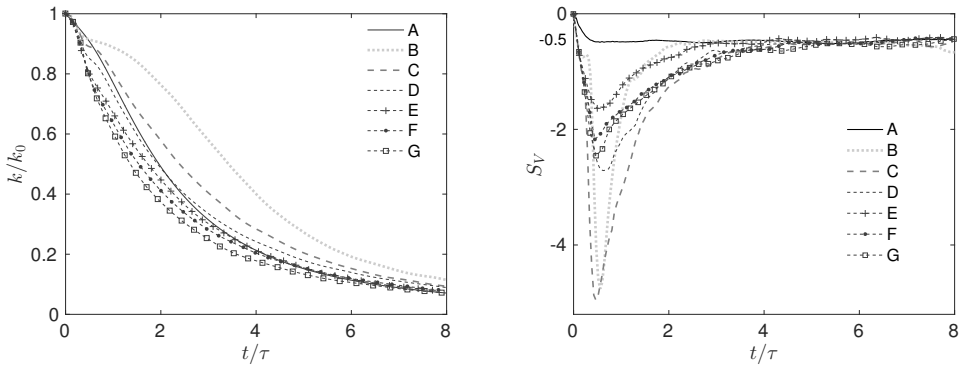

FIGURE 1. Evolution of (a) normalized turbulent kinetic energy k/k_0 and (b) velocity derivative skewness S_V, in Simulations A-G: (Table 1).

In figure 1(a) we present evolution of turbulent kinetic energy (k) observed in Simulations A-H. In figure 1(b), we present the evolution of skewness of the velocity derivative (S_V) which is defined as :

$$S_V = \frac{S_{V_{11}} + S_{V_{22}} + S_{V_{33}}}{3}; \tag{3.4}$$

where,

$$S_{V_{11}} = \frac{\overline{\left(\frac{\partial V_1'}{\partial x_1}\right)^3}}{\left[\overline{\left(\frac{\partial V_1'}{\partial x_1}\right)^2}\right]^{3/2}}, \ etc. \tag{3.5}$$

Note that the time in these figures have been normalized using τ, which represents eddy turnover time (Yeung & Pope 1989; Elghobashi & Truesdell 1992; Samtaney *et al.* 2001; Martín *et al.* 2006):

$$\tau = \frac{\lambda_0}{u_0'}; \tag{3.6}$$

where u_0' and λ_0 are the root mean square (rms) velocity and integral-length-scale of the initial flow field (at time, $t = 0$).

To obtain Lagrangian statistics, a Lagrangian particle tracker (LPT) is used to extract the full time-history of tagged fluid particles. Our LPT obtains the trajectory ($\mathbf{X}^+(\mathbf{y}, \mathbf{t})$) of a fluid particle by solving the following equation of motion:

$$\frac{\partial \mathbf{X}^+(t, \mathbf{y})}{\partial t} = \mathbf{V}\left(\mathbf{X}^+(t, \mathbf{y}), t\right), \tag{3.7}$$

where the superscript "+" represents Lagrangian flow variable, and $\mathbf{y}$ indicates the label/identifier assigned to the fluid particle at a reference time (t_{ref}). The initial value of $\mathbf{X}^+$ at a reference time is chosen at random. Using this initial condition, we then integrate (3.7) by employing second order Runge-Kutta method. However, upon integration, the position of the fluid particle at a subsequent time instant may not fall exactly on one of the grid points of computational domain used in the parent DNS. Therefore, an interpolation method is required to find relevant flow quantities at the particle's subsequent locations. Following the work of Yeung & Pope (1988), we choose cubic spline interpolation for

Simulation	Re_λ	M_t	Grid size	A_0	κ_0
A.	70	0.075	128^3	0.000023	4
B.	350	0.6	1024^3	0.0015	4
C.	150	1.0	512^3	0.0042	4
D.	100	1.0	512^3	0.0042	4
E.	70	1.0	256^3	0.0042	4
F.	70	1.25	256^3	0.0065	4
G.	70	1.5	256^3	0.0094	4

TABLE 1. Initial parameters of DNS simulations.

this purpose. Like our DNS solver, our LPT algorithm and implementation have been adequately validated (details are available in Danish *et al.* (2016*a*)).

4. Study I: Lagrangian investigations on the viscous process of velocity gradients

In this section we first examine the influence of compressibility on the exact process of velocity gradient dynamics (§4.1). Following a similar methodology, in §4.2 we examine the performance of the LLD model of Jeong & Girimaji (2003).

4.1. *DNS-based examination of viscous process*

The viscous process $\boldsymbol{\Upsilon}$ in the evolution equation of the velocity gradient tensor (2.7) is:

$$\Upsilon_{ij} = \underbrace{\nu \frac{\partial A_{ij}}{\partial x_k \partial x_k}}_{\Upsilon_{I_{ij}}} + \underbrace{\nu \frac{\partial A_{kk}}{\partial x_i \partial x_j}}_{\Upsilon_{II_{ij}}} - \underbrace{\frac{\nu}{\rho}\frac{\partial \rho}{\partial x_j}\left(\frac{\partial A_{ik}}{\partial x_k} + \frac{1}{3}\frac{\partial A_{kk}}{\partial x_i}\right)}_{\Upsilon_{III_{ij}}}. \tag{4.1}$$

In (4.1), $\Upsilon_{I_{ij}}$ and $\Upsilon_{II_{ij}}$ are essentially diffusion terms and $\Upsilon_{III_{ij}}$ is an interaction between density gradient and viscous process of the A_{ij} tensor. From the point of view of a dynamical equation of A_{ij} (like REE of Vieillefosse (1982) and/or EHEE of Suman & Girimaji (2009)), each of the three viscous terms ($\Upsilon_{I_{ij}}$, $\Upsilon_{II_{ij}}$ and $\Upsilon_{III_{ij}}$) represents a non-local, unclosed process.

To gauge the relative importance of these three constituent viscous processes, we define three fractions (f_I, f_{II}, f_{III}):

$$\begin{aligned}
f_I &= \frac{\sqrt{\Upsilon_{I_{ij}}\Upsilon_{I_{ij}}}}{\sqrt{\Upsilon_{I_{ij}}\Upsilon_{I_{ij}}} + \sqrt{\Upsilon_{II_{ij}}\Upsilon_{II_{ij}}} + \sqrt{\Upsilon_{III_{ij}}\Upsilon_{III_{ij}}}};\\
f_{II} &= \frac{\sqrt{\Upsilon_{II_{ij}}\Upsilon_{II_{ij}}}}{\sqrt{\Upsilon_{I_{ij}}\Upsilon_{I_{ij}}} + \sqrt{\Upsilon_{II_{ij}}\Upsilon_{II_{ij}}} + \sqrt{\Upsilon_{III_{ij}}\Upsilon_{III_{ij}}}},\\
f_{III} &= \frac{\sqrt{\Upsilon_{III_{ij}}\Upsilon_{III_{ij}}}}{\sqrt{\Upsilon_{I_{ij}}\Upsilon_{I_{ij}}} + \sqrt{\Upsilon_{II_{ij}}\Upsilon_{II_{ij}}} + \sqrt{\Upsilon_{III_{ij}}\Upsilon_{III_{ij}}}}.
\end{aligned} \tag{4.2}$$

Any of these fractions approaching unity can be used as an evidence of the corresponding process to be the dominant one. Using the flow-field at peak dissipation time from several simulations (B-G, Table 1), we have computed the volume-averaged values of f_I, f_{II} and f_{III}. We find that in all these simulations $f_I \approx 0.9$, $f_{II} \approx 0.09$ and $f_{III} \approx 0.01$. Based

on these findings, we conclude that for the range of Mach number and Reynolds number considered in this study, the exact process $\boldsymbol{\Upsilon}$ is almost solely represented by $\boldsymbol{\Upsilon_I}$, itself. Thus, in the rest of this study we focus only on $\boldsymbol{\Upsilon_I}$ and assume it to be synonymous with $\boldsymbol{\Upsilon}$.

Our interest is to examine how the viscous process $\boldsymbol{\Upsilon_I}$ undergoes change in comparison to its state at a reference time following a fluid particle. For monitoring this change we define an amplification ratio $r(t, t_{ref})$:

$$r(t, t_{ref}) = \frac{\sqrt{\Upsilon_{I_{ij}}(t)\Upsilon_{I_{ij}}(t)}}{\sqrt{\Upsilon_{I_{ij}}(t_{ref})\Upsilon_{I_{ij}}(t_{ref})}}, \tag{4.3}$$

where, $\Upsilon_{I_{ij}}(t)$ and $\Upsilon_{I_{ij}}(t_{ref})$ are values of the quantity $\Upsilon_{I_{ij}}$ associated with an identified fluid particle at an arbitrary time t and at the reference time t_{ref}, respectively. Since an individual particle represents just one realization, we obtain relevant statistics by calculating the mean of $r(t, t_{ref})$ over several identified fluid particles of a homogeneous flow field. The resulting quantity is referred to as $\langle r(t, t_{ref})\rangle$, and is truly a two-time Lagrangian correlation. Direct numerical simulation of compressible decaying turbulence along with our Lagrangian particle tracker (LPT) are employed to access $\langle r(t, t_{ref})\rangle$.

In this work fluid compressibility is parametrized based on the initial turbulent Mach number (3.3) and the locally normalized dilatation rate (a_{ii}). The normalized dilatation rate (a_{ii}) is the trace of the locally normalized velocity gradient tensor, which is defined as:

$$a_{ij} = A_{ij}/\sqrt{A_{mn}A_{mn}}. \tag{4.4}$$

The normalized dilatation-rate of a fluid particle (henceforth, referred to as just "dilatation") represents the normalized rate of change in density of a local fluid particle:

$$\frac{1}{\rho}\frac{d\rho}{dt'} = -a_{ii} \tag{4.5}$$

where $dt' = dt\sqrt{A_{ij}A_{ij}}$ represents time normalized with the local magnitude of the velocity gradient tensor itself. A positive value of a_{ii} implies an expanding fluid element, and a negative value of a_{ii} implies a contracting fluid element. A fluid particle with instantaneous $a_{ii} = 0$ implies a volume preserving fluid element. While the turbulent Mach number is a global/statistical indicator of compressibility, the normalized dilatation is a local parameter, and thus, it aptly represents the influence of compressibility on a specific local fluid particle. Note that a_{ii} is algebraically bounded between $\pm\sqrt{3}$.

To understand the influence of initial M_t on $\langle r(t, t_{ref})\rangle$, in figure 2 we present Lagrangian mean $\langle r(t, t_{ref})\rangle$ from simulations E-G. These simulations have identical initial Reynolds number (70) but different initial Mach numbers (1.00, 1.25, 1.50) In each of these simulations, the exact viscous process shows a two-stage evolution. In the first stage, $\langle r(t, t_{ref})\rangle$ increases and reaches a peak value. In the second stage, it has a monotonic decay. This evolution pattern is reminiscent of the evolution of dissipation itself. Indeed the time instant of the peak of dissipation and that of the viscous process almost match. The amplification in the first stage can be attributed to the steepening of gradients due to the rapid spread of the spectrum. The decay in the second stage of evolution can be related mainly to the decay in kinetic energy. We observe that as initial M_t increases, the peak value of $\langle r(t, t_{ref})\rangle$ also increases.

In several previous studies like Suman & Girimaji (2010) and Parashar *et al.* (2017*a*), it has been demonstrated that even when the unconditioned Eulerian or Lagrangian statistics obtained using DNS data of compressible homogeneous turbulence do not show any discernible influence of a global compressibility parameter like M_t, the same statistics

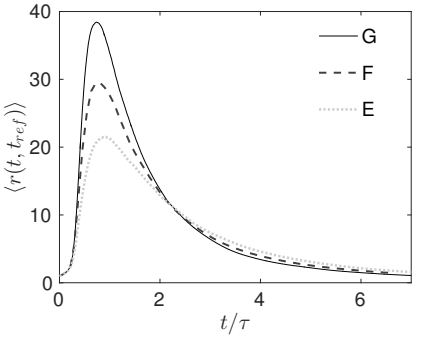

FIGURE 2. Mach number dependence on evolution of exact viscous term ($\langle r(t,t_{ref})\rangle$).

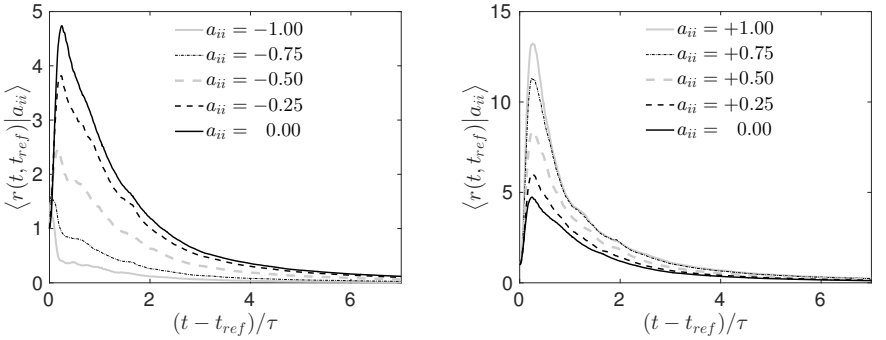

FIGURE 3. Dependence of $\langle r(t,t_{ref})|a_{ii}\rangle$ on a_{ii}. Results are from simulation G ($t_{ref} = 0.5\tau$).

when conditioned upon appropriate local compressibility parameters like normalized dilatation (a_{ii}) reveal significant variations and insightful physics. Examining the influence of local parameters like a_{ii} on turbulence processes is especially useful from the point of view of Lagrangian based statistical closure of turbulence (Lagrangian PDF methods, Pope (2002)), wherein dynamical equations are typically cast in terms of local flow variables directly. Thus to gain further insight into the viscous diffusion process ($\boldsymbol{\Upsilon_I}$), we subject $\langle r(t,t_{ref})\rangle$ to conditioned averaging on discrete values of a_{ii}.

In figure 3 we present conditional Lagrangian mean of $\langle r(t,t_{ref})\rangle$ from Simulation G, with a_{ii} at t_{ref} as the conditioning parameter. The reference time is chosen to be 0.5τ. In figure 3(a), separate curves are presented for $a_{ii} = -1.0, -0.75, -0.50, -0.25$ and 0, whereas in figure 3(b) separate curves are presented for $a_{ii} = +1.0, +0.75, +0.50, +0.25$ and 0. In both figures, we observe profound influence of both the magnitude and the sign of a_{ii} on the evolution of $\langle r(t,t_{ref})\rangle$. Even though almost at all dilatation levels the conditional mean, $\langle r(t,t_{ref})|a_{ii}\rangle$ seem to retain the two-stage evolution patterns as shown by the unconditioned statistics $\langle r(t,t_{ref})\rangle$, the extent to which the magnification of $\langle r(t,t_{ref})\rangle$ happens (figure 3) seems to be strongly affected by the value of a_{ii}. In figure 3(a) we observe that as the dilatation level changes from being zero (volume preserving fluid particles) to being more negative (contracting fluid particles), the peak value of $\langle r(t,t_{ref})|a_{ii}\rangle$ reduces. On the other hand, in figure 3(b) we observe the opposite trend: for fluid particles with high positive dilatation (fast expanding fluid particles) the peak value of $\langle r(t,t_{ref})|a_{ii}\rangle$ tends to increase.

In our attempt to understand and explain the behavior observed in figure 3(a) and 3(b), in figure 4(a) and 4(b) we present the mean value of the amplification of the magnitude of the velocity gradient tensor $\mathbf{A}$ itself, following the same set of fluid particles as used in figures 3. We measure this amplification as:

$$\langle r_A(t, t_{ref})\rangle = \left\langle \frac{A_{ij}(t)A_{ij}(t)}{A_{mn}(t_{ref})A_{mn}(t_{ref})} \right\rangle. \tag{4.6}$$

We observe that over almost the entire range of dilatation considered in this work, the trends shown by $\langle r_A(t, t_{ref})|a_{ii}\rangle$ are similar to $\langle r(t, t_{ref})|a_{ii}\rangle$. Like $\langle r(t, t_{ref})|a_{ii}\rangle$, a more positive dilatation tends to move the peak of $\langle r_A(t, t_{ref})|a_{ii}\rangle$ higher, and a more negative dilatation tends to lower the peak of $\langle r_A(t, t_{ref})|a_{ii}\rangle$. This similarity in the trends shown by $\langle r(t, t_{ref})|a_{ii}\rangle$ in figure 3 and that shown by $\langle r_A(t, t_{ref})|a_{ii}\rangle$ in figure 4 is not completely unexpected, and it indeed substantiates a gradient diffusion like hypothesis which assumes $\boldsymbol{\Delta}\mathbf{A} \propto \mathbf{A}$ (Martín *et al.* 1998; Jeong & Girimaji 2003). However, in the light of figure 4(a) and 4(b) our primary curiosity that why the peaks of $\langle r(t, t_{ref})\rangle$ (in figure 3(a) and 3(b)) rise for expanding fluid particles and reduce for contracting fluid particles can now possibly be explained. In figure 5 we show $\left\langle \sqrt{A_{ij}A_{ij}}\middle|a_{ii}\right\rangle$ at three time instants, t_{ref}, $t_{ref} + \tau/4$ and $t_{ref} + \tau/2$ (We observe that the one time statistics of $\left\langle \sqrt{A_{ij}A_{ij}}\middle|a_{ii}\right\rangle$ does not show significant variations with time). The dependence of $\left\langle \sqrt{A_{ij}A_{ij}}\middle|a_{ii}\right\rangle$ on a_{ii} is monotonic and almost linear for $a_{ii} > 0$. A faster expanding fluid particle (large positive a_{ii}) is associated with smaller $\left\langle \sqrt{A_{ij}A_{ij}}\middle|a_{ii}\right\rangle$ than a slower expanding fluid particle (small positive a_{ii}). On the other hand contracting particles show a more complex behavior. Extremely fast contracting particles (very high negative a_{ii}) have a very large $\left\langle \sqrt{A_{ij}A_{ij}}\middle|a_{ii}\right\rangle$. As dilatation becomes less negative $\left\langle \sqrt{A_{ij}A_{ij}}\middle|a_{ii}\right\rangle$ drops first (till $a_{ii} \approx -0.25$) and then again tends to be larger. Thus the dependence of $\left\langle \sqrt{A_{ij}A_{ij}}\middle|a_{ii}\right\rangle$ on a_{ii} is non-monotonic as well as (apparently) non-linear (figure 5). In figure 6(a) we present the averaged rate of change in dilatation (ψ) of tagged fluid particles over one Kolmogorov time:

$$\psi = \left\langle \frac{(a_{ii}(\tau_\kappa + t_{ref}) - a_{ii}(t_{ref}))}{\tau_\kappa} \right\rangle; \tag{4.7}$$

where, τ_κ is the Kolmogorov time at t_{ref}. In figure 6(b) we present the fraction of particles having increased/decreased their a_{ii} over one Kolmogorov time relative to the dilatation the particles had at t_{ref}. We observe that expanding par ticles are associated with negative ψ and contracting particles are associated with positive ψ. In other words, both contracting and expanding fluid particles tend to reduce the magnitudes of their dilatation. Thus particles with higher initial positive dilatation tend to acquire lower positive dilatation levels. Further, since the associated $\left\langle \sqrt{A_{ij}A_{ij}}\middle|a_{ii}\right\rangle$ of particles with higher positive dilatation is smaller than those with lower positive dilatation (figure 4), it is plausible to expect that the peak of $\langle r(t, t_{ref})\rangle$ will be more for higher positive a_{ii} than that for lower positive a_{ii}. Indeed this behavior is observed in figure 3(b).

For contracting particles the dynamics seem to be more complicated because of non-monotonic and highly non-linear distribution of $\left\langle \sqrt{A_{ij}A_{ij}}\middle|a_{ii}\right\rangle$ (figure 5). At low negative dilatation (say $aii \approx -0.25$), the dominant tendency of particles is to move towards zero dilatation (figure 6). The association of higher $\left\langle \sqrt{A_{ij}A_{ij}}\middle|a_{ii}\right\rangle$ at zero dilatation compared to that at low negative dilatation (figure 5) still allows $\langle r_A(t, t_{ref})|a_{ii}\rangle$ to show a substantial magnification at early times (figure 4(a)).

For faster contracting particles (say those with initial $a_{ii} \approx -0.75$), figure 6 shows that (like other contracting particles) they begin their journey towards zero dilatation. However, figure 5 suggests that as their dilatation reduces, $\left\langle \sqrt{A_{ij}A_{ij}}\middle|a_{ii}\right\rangle$ severely drops.

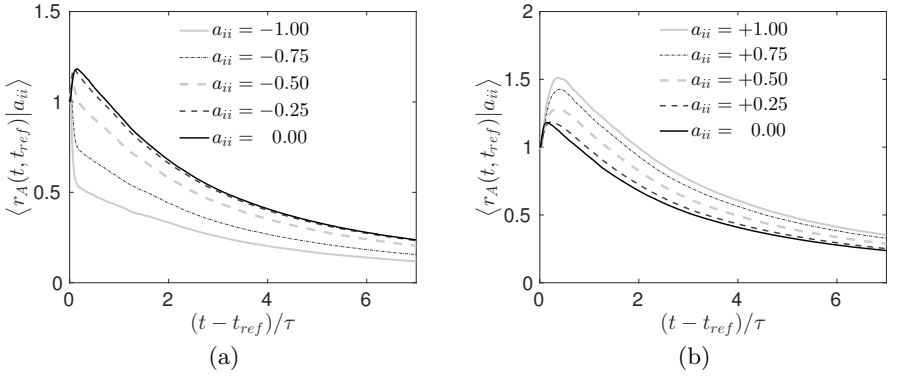

FIGURE 4. Dependence of $\langle r_A(t,t_{ref})|a_{ii}\rangle$ on a_{ii}. Results are from simulation G ($t_{ref} = 0.5\tau$).

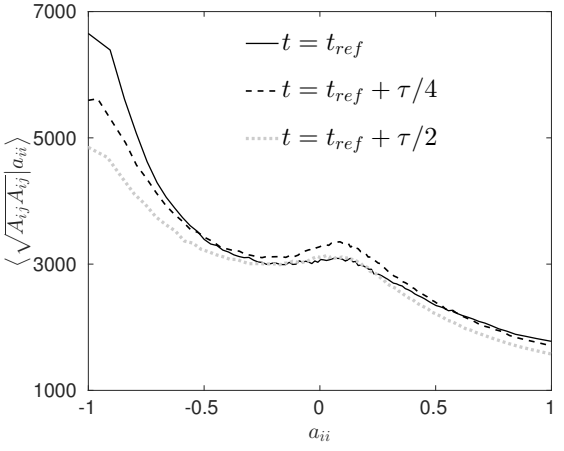

FIGURE 5. $\langle\sqrt{A_{ij}A_{ij}}|a_{ii}\rangle$ vs a_{ii} at different time instants for Simulation G ($t_{ref} = 0.5\tau$).

This decreasing tendency, combined with the fact that initially they had a higher value of $\langle\sqrt{A_{ij}A_{ij}}|a_{ii}\rangle$, results into a dramatic drop in $\langle r_A(t,t_{ref})|a_{ii}\rangle$ as observed in figure 4(a).

In the light of the foregoing discussion we now make an attempt to explain the influence of initial turbulent Mach number observed in figure 2. It is known that as initial M_t is increased, more particles tend to have non-zero dilatation, and also larger magnitudes of normalized dilatation are generated (Suman & Girimaji 2009; Lee *et al.* 2009). In figure 7(a) we show pdf of dilatation at the peak dissipation time in Simulation E−G. We observe that (i) the population of fast expanding particles as well as the fast contracting particles increase as the initial turbulent Mach number is increased, and (ii) the population distribution is almost symmetric on the positive and the negative a_{ii} sides. In figure 7(b) we present $\langle r_A(t,t_{ref})|a_{ii}\rangle$ at peak dissipation from simulations E−G. We observe that as initial M_t increases, the disparity of $\langle r_A(t,t_{ref})|a_{ii}\rangle$ across a_{ii} increases. This explains the increase in peak of $\langle r(t,t_{ref})\rangle$ observed in figure 2.

4.2. *Evaluation of the LLD model*

Having examined the behavior of the exact process $\boldsymbol{\Upsilon_I}$ we examine the performance of the LLD model of Jeong & Girimaji (2003), which intends to capture the essential physics

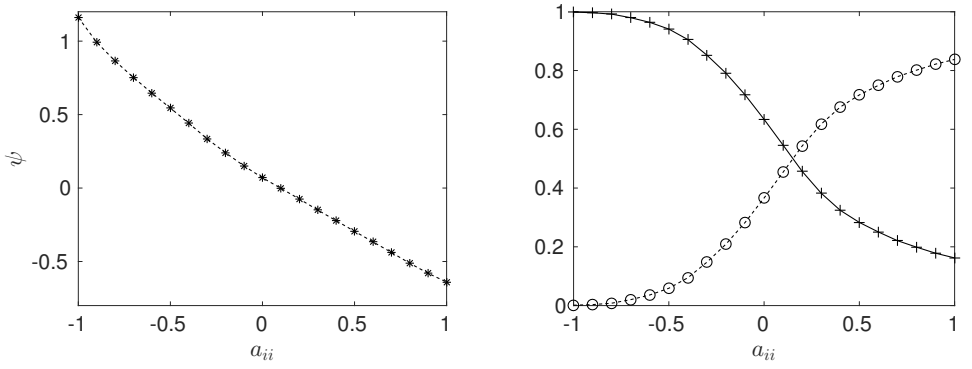

FIGURE 6. (a) ψ vs a_{ii} at $t_{ref} = 0.5\tau$. (b) Fraction of particles moving towards +ve a_{ii} (symbol +) and -ve a_{ii} (symbol o).

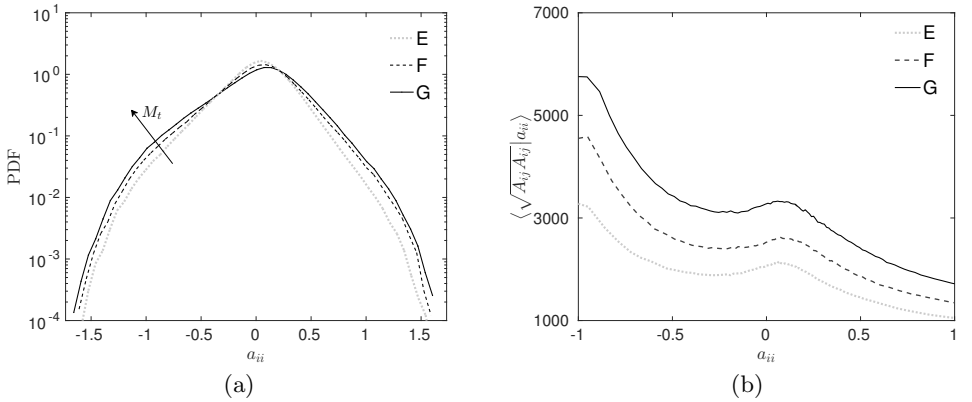

FIGURE 7. (a) PDF of a_{ii} for Simulations E−G. (b) $\langle \sqrt{A_{ij}A_{ij}} | a_{ii} \rangle$ vs a_{ii} for Simulations E−G.

of this exact process. The primary motivation of Jeong & Girimaji (2003) to develop the LLD model was to ensure that the viscous process is large enough to eliminate the finite time singularity problem seen earlier in the restricted Euler dynamics Cantwell & Coles (1983). While the LLD model was found to achieve this requirement by quickly amplifying the modeled expression of the viscous action using the trace of the Cauchy-Green tensor, the exact nature of the modeled expression and other time-dependent aspects remain questionable−especially its anticipated exponential growth at late times (see comments by Chevillard *et al.* (2003)). In this work we pursue a detailed examination of the behavior of the LLD model following fluid particles and employing the exact DNS flow field in the background. For this examination, we use the results of two simulations: A and G. Both these simulations have the same initial Reynolds number (70) but different Mach numbers. Simulation A with initial $M_t = 0.075$ can be treated as almost incompressible, while Simulation G has considerable compressibility with initial $M_t = 1.5$.

The LLD modeling approach of Jeong & Girimaji (2003) uses Lagrangian-Eulerian change in variables to cast $\Upsilon_{I_{ij}}$ as:

$$\nu \frac{\partial^2 A_{ij}}{\partial x_k \partial x_k} = \nu \frac{\partial}{\partial x_k} \left(\frac{\partial X_m}{\partial x_k} \frac{\partial A_{ij}}{\partial X_m} \right), \tag{4.8}$$

where, X_i and x_i are Eulerian and Lagrangian spatial co-ordinates. Further expansion of rhs of (4.8) leads to:

$$\nu\frac{\partial^2 A_{ij}}{\partial x_k \partial x_k} = \underbrace{\nu\frac{\partial X_n}{\partial x_k}\frac{\partial X_m}{\partial x_k}\frac{\partial^2 A_{ij}}{\partial X_m \partial X_n}}_{A} + \underbrace{\nu\frac{\partial A_{ij}}{\partial X_m}\frac{\partial^2 X_m}{\partial x_k \partial x_k}}_{B}. \tag{4.9}$$

Jeong & Girimaji (2003) neglects Term B (first modeling assumption) on the rhs of (4.9) to arrive at the following:

$$\nu\frac{\partial^2 A_{ij}}{\partial x_k \partial x_k} \approx \nu\frac{\partial X_n}{\partial x_k}\frac{\partial X_m}{\partial x_k}\frac{\partial^2 A_{ij}}{\partial X_m \partial X_n}. \tag{4.10}$$

Using the definition of the deformation gradient tensor $D_{ij} = \frac{\partial x_i}{\partial X_j}$ and the right Cauchy-Green tensor $C_{ij} = D_{km}D_{kn}$, the rhs of (4.10) can be expressed in terms of the tensor $\mathbf{C}$:

$$\nu\frac{\partial^2 A_{ij}}{\partial x_k \partial x_k} \approx \nu C^{-1}_{mn}\frac{\partial^2 A_{ij}}{\partial X_m \partial X_n} \tag{4.11}$$

Further, Jeong & Girimaji (2003) make the second modeling assumption wherein $\mathbf{C^{-1}}$ is approximated to be an isotropic tensor:

$$\nu\frac{\partial^2 A_{ij}}{\partial x_k \partial x_k} \approx \nu\frac{C^{-1}_{kk}}{3}\delta_{mn}\frac{\partial^2 A_{ij}}{\partial X_m \partial X_n}; \tag{4.12}$$

which leads to:

$$\nu\frac{\partial^2 A_{ij}}{\partial x_k \partial x_k} \approx \nu\frac{C^{-1}_{kk}}{3}\frac{\partial^2 A_{ij}}{\partial X_m \partial X_m}. \tag{4.13}$$

Finally, the third approximation is made: $\frac{\partial^2 A_{ij}}{\partial X_m \partial X_m} \approx -\frac{A_{ij}}{\tau_L}$, leading to the final form of the so called Lenear Lagrangian Diffusion (LLD) model:

$$\nu\frac{\partial^2 A_{ij}}{\partial x_k \partial x_k} \approx -\frac{1}{\tau_L}\frac{C^{-1}_{kk}}{3}A_{ij}. \tag{4.14}$$

Jeong & Girimaji (2003) consider the quantity τ_L to be a constant and interpret this as a molecular viscous relaxation time scale. This model has been employed by Jeong & Girimaji (2003) to close the restricted Euler equation (REE). Later, Suman & Girimaji (2012) have employed it to capture the physics of viscous diffusion process in the enhanced Homogenized Euler equation (EHEE) model, which is the counterpart of REE for compressible flows.

While introducing their *recent fluid formation closure* hypothesis, Chevillard & Meneveau (2006) employed almost the same final form for the viscous process as proposed by Jeong & Girimaji (2003), however, they rationalized the model using a different set of arguments. First, instead of assuming the $\mathbf{C^{-1}}$ tensor to be isotropic, the authors assumed the fourth-order tensor $\frac{\partial^2 A_{ij}}{\partial X_m \partial X_n}$ (Lagrangian Hessian of the tensor $\mathbf{A}$) to be isotropic, and thereafter expressed it in terms of the tensor A_{ij} and a length scale δX associated with the flow field at t_{ref}:

$$\frac{\partial^2 A_{ij}}{\partial X_m \partial X_m} \approx -C^{-1}_{mn}\frac{A_{ij}}{(\delta X)^2}\frac{\delta_{mn}}{3}. \tag{4.15}$$

Subsequently, (4.15) when combined with (4.11) then leads to the following form:

$$\nu \frac{\partial^2 A_{ij}}{\partial x_k \partial x_k} \approx -\nu \frac{C_{kk}^{-1}}{3} \frac{A_{ij}}{(\delta X)^2}; \tag{4.16}$$

Chevillard & Meneveau (2006) interpret δX as the characteristic length scale that a fluid particle traverses over a Kolmogorov timescale, and thus $\delta X \approx \lambda$, where λ is the Taylor-microscale of the turbulent flow field at the reference time t_{ref}. Thus, the final version of the LLD model takes the form:

$$\nu \frac{\partial^2 A_{ij}}{\partial x_k \partial x_k} \approx -\frac{\nu}{\lambda^2} \frac{C_{kk}^{-1}}{3} A_{ij}. \tag{4.17}$$

As mentioned in the Introduction, with access to the DNS data of decaying turbulence and a validated Lagrangian particle tracker, we now intend to scrutinize the performance of this model (4.17). For this study, we select the same set of particles that we used in §4.1 to examine the exact $\boldsymbol{\Upsilon_I}$. Following these particles we calculate $C_{kk}^{-1} \frac{\nu}{3\lambda^2} A_{ij}$. Like the exact process (4.3), we define the amplification ratio of the modeled viscous process as:

$$r_m\left(t, t_{ref}\right) = \frac{\left(\frac{C_{kk}^{-1}}{3}\sqrt{A_{ij}A_{ij}}\right)_t}{\left(\frac{C_{kk}^{-1}}{3}\sqrt{A_{ij}A_{ij}}\right)_{t_{ref}}} = \frac{\left(C_{kk}^{-1}\sqrt{A_{ij}A_{ij}}\right)_t}{\left(\sqrt{A_{ij}A_{ij}}\right)_{t_{ref}}} \tag{4.18}$$

At each time instant the ratio $r_m(t, t_{ref})$ is calculated, and subsequently the mean value $\langle r_m(t, t_{ref})\rangle$ is computed by taking averages across the identified set of particles. A direct comparison of $\langle r_m(t, t_{ref})\rangle$ is then performed against $\langle r(t, t_{ref})\rangle$. Note that to find C_{kk}^{-1} at any arbitrary time we use the following exact evolution equation of deformation gradient tensor D_{ij} (Jeong & Girimaji 2003):

$$\frac{dD_{ij}}{dt} = D_{ik}A_{kj}, \tag{4.19}$$

where, both $\mathbf{A}$ and $\mathbf{D}$ are calculated using the DNS data fields at different time instants and the Lagrangian particle tracker. Thus, our evaluation procedure uses the exact instantaneous states of the $\mathbf{A}$ and the $\mathbf{C}$ tensors as provided by DNS.

In figure 8(a), we present evolution of both $\langle r_m(t, t_{ref})\rangle$ and $\langle r(t, t_{ref})\rangle$ using results of simulation A (nearly incompressible with initial M_t being 0.075 and Re_λ=70). In figure 8(b), results are shown using DNS data from Simulation G (highly compressible with initial M_t being 1.5 and Re_λ=70). In each case $t_{ref} = 0$. We observe that in both simulations, unlike the evolution of the exact process, the LLD model shows monotonic growth with time. At the early stages of evolution, this monotonic growth is at least qualitatively similar to the exact process. However, at later stages (after the dissipation peak) the continued monotonic growth of $\langle r_m(t, t_{ref})\rangle$ is in gross disagreement with $\langle r(t, t_{ref})\rangle$, which shows a decaying behavior in the second stage. Our results clearly show that even though the LLD model may eliminate the problem of finite time singularity of the restricted Euler equation (Jeong & Girimaji 2003), its growth, especially at late times, is unrealistic and severely overestimates the strength of the actual viscous process in both incompressible and compressible flow fields.

In an attempt to diagnose the problems of the LLD model (4.17), we revisit the LLD modeling procedure of Jeong & Girimaji (2003) and Chevillard & Meneveau (2006). To begin with, we avoid the assumptions made by Chevillard & Meneveau (2006) regarding the isotropic structure of the fourth-order tensor $\frac{\partial^2 A_{ij}}{\partial X_m \partial X_n}$. Instead, we approximate the

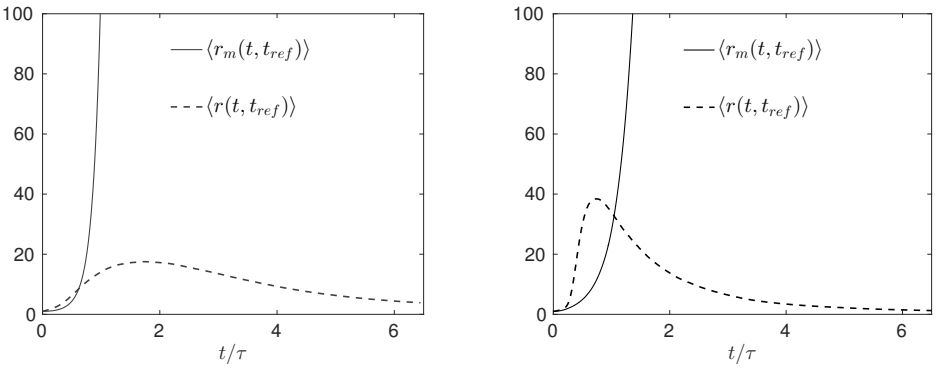

FIGURE 8. Comparison of $\langle r(t,t_{ref})\rangle$ and $\langle r_m(t,t_{ref})\rangle$: (a) Simulation A (nearly incompressible), (b) Simulation G (compressible).

Lagrangian Hessian of A_{ij} as:

$$\frac{\partial^2 A_{ij}}{\partial X_m \partial X_n} \approx \frac{A_{ij}}{(\delta X)^2} R_{mn}; \tag{4.20}$$

where, δX is the same length scale as described by Chevillard & Meneveau (2006). In (4.20) the symbol R_{mn} represents the $(m-n)^{th}$ component of a second-order tensor, which is no more necessarily an isotropic tensor as assumed by Chevillard & Meneveau (2006). Now combining (4.20) with (4.11), we arrive at:

$$\nu \frac{\partial^2 A_{ij}}{\partial x_k \partial x_k} \approx \nu C^{-1}_{mn} \frac{\partial^2 A_{ij}}{\partial X_m \partial X_n} \approx -\nu C^{-1}_{mn} \frac{A_{ij}}{(\delta X)^2} R_{mn} \tag{4.21}$$

Equation (4.21) has so far been written in terms of the components of various tensors using a coordinate system fixed to the laboratory. The equation can be readily expressed in its full tensor form as:

$$\nu \nabla^2 \mathbf{A} \approx -\frac{\nu}{(\delta X)^2} \left(\mathbf{C} : \mathbf{R}\right) \mathbf{A} \tag{4.22}$$

If we now express $\mathbf{C^{-1}}$ and $\mathbf{R}$ tensors in the eigen-system of the instantaneous $\mathbf{C^{-1}}$ tensor, then (4.22) can be expressed as:

$$\nu \nabla^2 \mathbf{A} \approx -\frac{\nu}{(\delta X)^2} \left(\alpha R_\alpha + \beta R_\beta + \gamma R_\gamma\right) \mathbf{A} \tag{4.23}$$

where, α, β and γ are the three eignevalues of the instantaneous $\mathbf{C^{-1}}$ sorted as $\alpha \geqslant \beta \geqslant \gamma$, and these symbols when sub-scripted, imply the component of a tensor along the corresponding eigenvector.

Our DNS results from both nearly incompressible and compressible cases show that $\mathbf{C^{-1}}$ tensor evolves to a state with its largest eigenvalue being overwhelmingly dominant over the other two. figure 9 show the instantaneously normalized eigenvalues of $\mathbf{C^{-1}}$ from Simulation A and G. The plotted quantities T_α, T_β and T_γ are defined as:

$$T_\alpha = \frac{\alpha^2}{\alpha^2 + \beta^2 + \gamma^2};$$
$$T_\beta = \frac{\beta^2}{\alpha^2 + \beta^2 + \gamma^2};$$

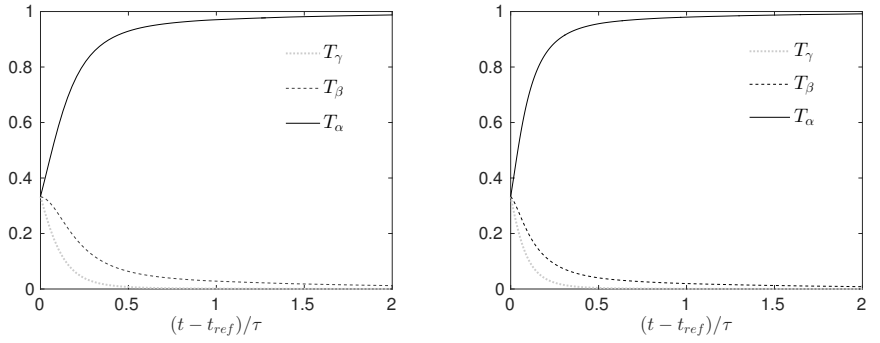

FIGURE 9. Evolution of T_α, T_β and T_γ in (a) Simulation A (nearly incompressible, (b) Simulation G (compressible).

$$T_\gamma = \frac{\gamma^2}{\alpha^2 + \beta^2 + \gamma^2}; \tag{4.24}$$

Similar findings from incompressible simulations have been reported earlier as well Girimaji & Pope (1990*a*). Since the order of magnitude of the Lagrangian Hessian in (4.23) is essentially represented by $A_{ij}/\delta X^2$, we expect the magnitude of the components of $\mathbf{R}$ to either close to zero or of order unity. Thus it is plausible to approximate (4.23) as:

$$\nu\nabla^2\mathbf{A} \approx -\frac{\nu}{(\delta X)^2}\left(\alpha R_\alpha + \beta R_\beta + \gamma R_\gamma\right)\mathbf{A} \approx -\frac{\nu}{(\delta X)^2}\left(\alpha R_\alpha\right)\mathbf{A} \tag{4.25}$$

Now, adopting the interpretation offered by Chevillard & Meneveau (2006) for the quantity $\delta X \approx \lambda$, (4.25) can be expressed as:

$$\nu\nabla^2\mathbf{A} \approx -\frac{\nu}{\lambda^2}\left(\alpha R_\alpha\right)\mathbf{A} \tag{4.26}$$

At this point we compare (4.26) and the form of the model used by Chevillard & Meneveau (2006) (4.17). Taking into account that the DNS behaviour shows $|\alpha| >> |\beta|, |\gamma|$, the approximation made in (4.25) can also be applied to (4.17). This will reduce (4.17) to:

$$\nu\nabla^2\mathbf{A} \approx -\frac{\nu}{\lambda^2}\left(\alpha\frac{1}{3}\right)\mathbf{A} \tag{4.27}$$

Thus, the essential difference between the modified model (4.26) and the original LLD model (4.17) is that while the original model has already committed to R_α being 1/3, the modified model has not imposed any such restriction so far.

Given that α is known to grow exponentially, and the fact that (4.27) leads to gross overestimation of growth of $\langle r_m(t, t_{ref})\rangle$ (figure 8), we conjecture that the quantity R_α must follow an exponential decay towards zero (4.28), so as to restrain the unrealistic growth of $\langle r_m(t, t_{ref})\rangle$ in comparison to the expected behavior represented by $\langle r(t, t_{ref})\rangle$:

$$R_\alpha \approx |\alpha|^{-m} \tag{4.28}$$

The exponent m, however, is expected to be a time varying quantity dependent on the instantaneous as well as the history of the fluid particle being followed. The role of m is to provide an exponential modulation, so that the exponential growth shown by the original LLD model (4.17) displayed in figure 8 can be reined in. At this point we present (4.28) merely as a modeling proposal. More detailed analysis and probably DNS data

Acronyms	$p = 0$	$p < 0$	$p > 0$	Eigenvalues of a_{ij}
SFS	$r < 0$	$r < 0$ & $S2 > 0$	$r < 0$	complex
UFC	$r > 0$	$r > 0$	$r > 0$ & $S2 < 0$	complex
UNSS	$r > 0$ & $q < 0$	$r > 0$	$r > 0$ & $q < 0$	real
SNSS	$r < 0$ & $q < 0$	$r < 0$ & $q < 0$	$r < 0$	real
UFS	—	$r < 0$ & $S2 < 0$	—	complex
UN/UN/UN	—	$r < 0$ & $q > 0$	—	real
SFC	—	—	$r > 0$ & $S2 > 0$	complex
SN/SN/SN	—	—	$q > 0$ & $r > 0$	real

TABLE 2. Zones of various topologies on $p - q - r$ space, where acronyms are: stable-focus-stretching (SFS), unstable-focus-compressing (UFC), unstable-node/saddle/saddle (UNSS), stable-node/saddle/saddle (SNSS), unstable-focus-stretching (UFS), unstable-node/unstable-node/unstable-node (UN/UN/UN), stable-focus-compressing (SFC), stable-node/stable-node/stable-node (SN/SN/SN).

over a wide range of Mach number and Reynolds number will be required to arrive at a concrete functional form of m. Such an effort, however, is outside the scope of the present work.

5. Study II: Lagrangian investigation of dynamics of velocity gradient invariants

The topology associated with a fluid element is the local streamline pattern in its vicinity as observed with respect to a reference frame which is purely translating with the center of mass of the fluid element. Topology depends on the nature of eigenvalues of the local state of the velocity gradient tensor. However, it can also be inferred with a knowledge of the three invariants (P, Q, R) of the velocity gradient tensor :

$$P = -A_{ii}, Q = \frac{1}{2}\left(P^2 - A_{ij}A_{ji}\right), and$$
$$R = \frac{1}{3}\left(-P^3 + 3PQ - A_{ij}A_{jk}A_{ki}\right). \tag{5.1}$$

Correspondingly, the locally normalized invariants (p,q,r) of the local velocity gradient tensor (a_{ij}) are defined in terms of the normalized velocity gradient tensor (a_{ij}):

$$p = -a_{ii}, q = \frac{1}{2}\left(p^2 - a_{ij}a_{ji}\right), \ and$$
$$r = \frac{1}{3}\left(-p^3 + 3pq - a_{ij}a_{jk}a_{ki}\right). \tag{5.2}$$

Chen *et al.* (1989) categorize topological patterns (Table 2) of an incompressible field into unstable-node-saddle-saddle (UNSS), stable-node-saddle-saddle (SNSS), stable-focus-stretching (SFS), and unstable-focus-compressing (UFC). In compressible flows, additional four more major topologies can exist: stable-focus-stretching (SFS) and stable-node/stable-node/stable-node(SNSNSN), which are associated with contracting fluid particles; and unstable-focus-stretching (UFS) and unstable-node/unstable-

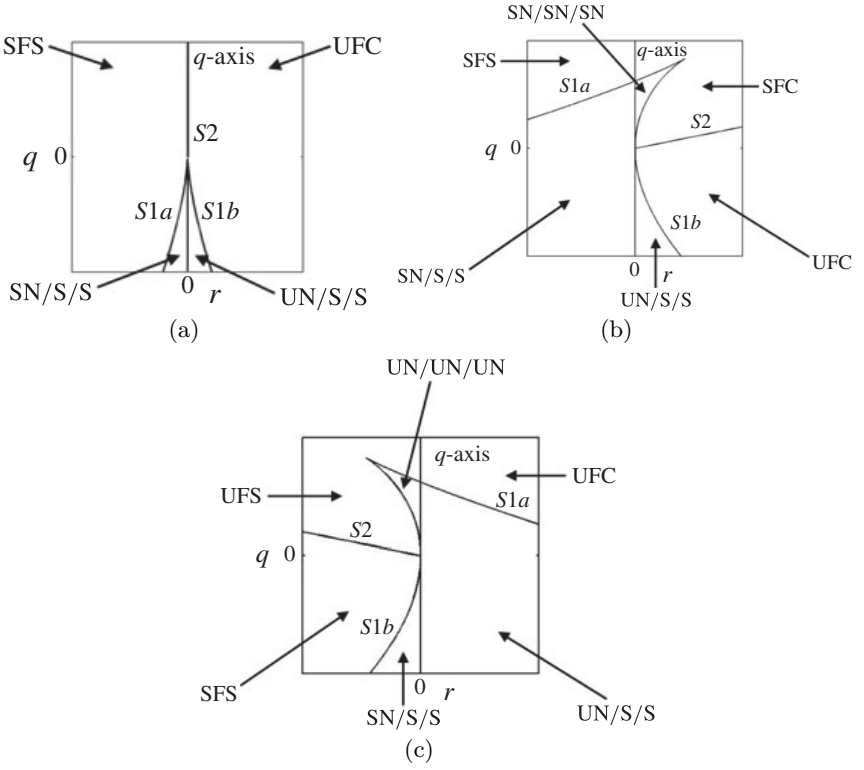

FIGURE 10. Regions of different flow topologies in different p-planes: (a) $p = 0$, (b) $p > 0$ and (c) $p < 0$.)

node/unstable-node (UNUNUN), which are associated with expanding fluid particles. Figure 10 shows different regions in the $p-q-r$ space associated with different topologies. The reader is referred to Chong *et al.* (1990) for further details on topology. Since the value of the three invariants of the velocity gradient tensor uniquely determines the topology associated with a local fluid element, the dynamics of topology can be studied in terms of the dynamics of invariants themselves.

Using the evolution equation of the velocity-gradient-tensor (2.7), the time-evolution of invariants (P,Q,R) can be expressed Bechlars & Sandberg (2017):

$$\begin{aligned}
\frac{dP}{dt} &= P^2 - 2Q - S_{ii};\\
\frac{dQ}{dt} &= QP - \frac{2P}{3}S_{ii} - 3R - A_{ij}S^*_{ji};\\
\frac{dR}{dt} &= -\frac{Q}{3}S_{ii} + PR - PA_{ij}S^*_{ji}) - A_{ik}A_{kj}S^*_{ji};
\end{aligned} \tag{5.3}$$

where, S_{ij} is the source term in the evolution equation of velocity-gradient-tensor (2.7) and the symbol S^*_{ij} is the traceless part of the S_{ij} tensor:

$$\begin{aligned}
S_{ij} &= -\mathbb{P}_{ij} + \Upsilon_{ij};\ \textit{and}\\
S^*_{ij} &= S_{ij} - \frac{S_{kk}}{3}\delta_{ij}.
\end{aligned} \tag{5.4}$$

Here $\mathbb{P}_{ij}$ is the pressure hessian tensor and Υ_{ij} represents the viscous process in the evolution equation of the velocity-gradient tensor (2.7).

The relationship between the non-normalized invariants (P,Q,R) and normalized invariants (p,q,r) is:

$$p = \frac{P}{\sqrt{A_{ij}A_{ij}}}, q = \frac{Q}{A_{ij}A_{ij}}, \text{ and } r = \frac{R}{(A_{ij}A_{ij})^{3/2}} \tag{5.5}$$

Using (5.3) and the relationship (5.5), the evolution equation of the normalized invariants (p,q,r) can be derived as:

$$\begin{aligned}
\frac{dp}{dt} &= \frac{d}{dt}\left(\frac{P}{\sqrt{A_{ij}A_{ij}}}\right) = \frac{1}{\sqrt{A_{ij}A_{ij}}}\frac{dP}{dt} - \frac{P}{(A_{ij}A_{ij})^{3/2}}A_{ij}\frac{dA_{ij}}{dt}, \\
\frac{dq}{dt} &= \frac{d}{dt}\left(\frac{Q}{A_{ij}A_{ij}}\right) = \frac{1}{A_{ij}A_{ij}}\frac{dQ}{dt} - \frac{2Q}{(A_{ij}A_{ij})^{2}}A_{ij}\frac{dA_{ij}}{dt}, \\
\frac{dr}{dt} &= \frac{d}{dt}\left(\frac{R}{(A_{ij}A_{ij})^{3/2}}\right) = \frac{1}{(A_{ij}A_{ij})^{3/2}}\frac{dQ}{dt} - \frac{3R}{(A_{ij}A_{ij})^{5/2}}A_{ij}\frac{dA_{ij}}{dt}.
\end{aligned} \tag{5.6}$$

While following an identified fluid particle in physical space and tracking its invariants information, we can track the footprints of the fluid particle in the p-q-r space as well. We refer to such a trajectory of the fluid particle in *p-q-r* space as the Lagrangian trajectory (LT).

5.1. *Lifetime of topology*

One of the central questions to address while studying the dynamics of velocity gradients and flow field topology is how long a topology lasts and how compressibility influences that. In this section we address this question. We quantify the lifetime of a topology as the time it takes for a fluid particle to change its topology relative to the topology it had at a reference time t_{ref}. We express this time non-dimensionalized by the Kolmogorov time scale (τ_κ) of the homogeneous flow field at t_{ref}. We refer to the normalized lifetime of a given topology ($\mathcal{T}$) thus obtained as $L_\mathcal{T}$:

$$L_\mathcal{T} = \frac{t^* - t_{ref}}{\tau_\kappa}; \tag{5.7}$$

where t^* denotes the time instant when the original topology $\mathcal{T}$ associated with a tagged fluid particle changes to some other topology. Correspondingly, the mean value of $L_\mathcal{T}$ is calculated by following a large number of tagged particles which have the same topology $\mathcal{T}$ at t_{ref}:

$$\langle L_\mathcal{T} \rangle = \frac{\langle t^* - t_{ref} \rangle}{\tau_\kappa}. \tag{5.8}$$

In all our calculations and analysis of lifetime of topologies we employ the data fields of Simulation A-E and G, and in each case $t_{ref} = 4\tau$. The sample sizes used for calculating the mean lifetime of topologies ranges between $50,000 - 300,000$. To identify the rolw of compressibility on lifetimes, we also examine $\langle L_\mathcal{T} \rangle$ conditioned upon discrete values of a_{ii} of the reference time (t_{ref}). These conditioned lifetimes are represented as $\langle L_\mathcal{T} | a_{ii} \rangle$.

In figure 11 we present mean lifetimes of various topologies conditioned upon different initial dilatation levels: $\langle L_\mathcal{T} | a_{ii} \rangle$. Each sub-figure corresponds to a specific topology. The six major topologies that exist in compressible turbulence are considered (UNSS, SNSS, SFC, SFS, UFC and UFS). Further, to identify the role of initial turbulent Mach number M_t, we have calculated $\langle L_\mathcal{T} | a_{ii} \rangle$ using Simulations xx. These simulations have identical initial Reynolds number (70), but different initial Mach number (1.00. 1.25 and 1.5).

We observe that the compressibility parameters−dilatation and initial Mach numbers

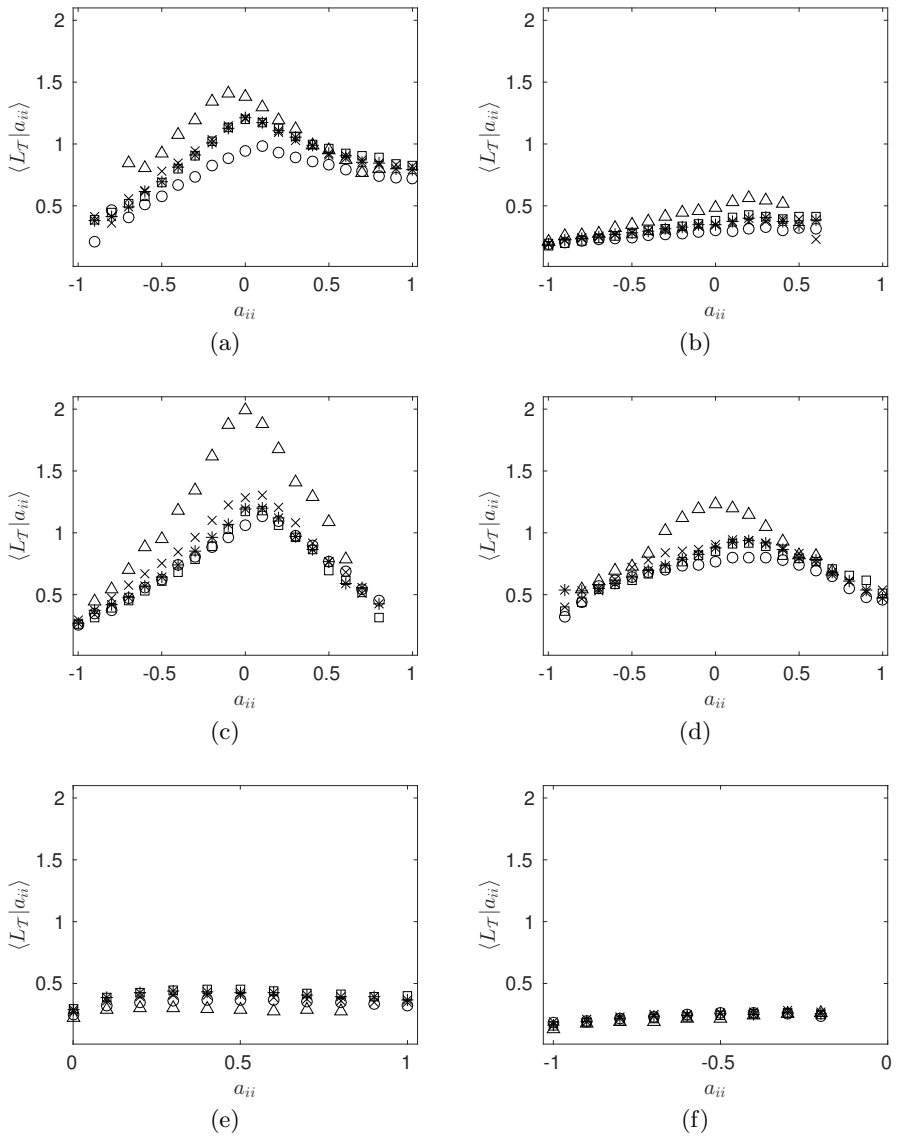

FIGURE 11. $L_{\mathcal{T}|a_{ii}}$ from different simulations (bin size: $\overline{a_{ii}} \pm 0.05$) for 6 major topologies: (a) UNSS, (b) SNSS, (c) SFS, (d) UFC, (e) UFS and (f) SFC. Symbol △, □, ∗, ×, and O represents life-time of topology for simulations B, C, D, E and G respectively.

influence the lifetimes of some topologies selectively. Mean lifetimes of UNSS (figure 11(a)), UFC (figure 11(c)) and SFS figure 11(d)) topologies seem to be significantly more sensitive to both the Mach number and dilatation compared to those of the other topologies. As the level of dilatation increases from high negative values to zero dilatation, lifetimes of these topologies increase. On the other side, however, as we move from zero to positive dilatation, lifetimes seem to decrease again. An increase in initial Mach number seems to pronounce these variations more as evident in figures 11 a, c, and d. In contrast to UNSS, UFC and SFS topologies the other three major topologies exiting in a compressible

p ($-a_{ii}$)	UNSS	SNSS	SFS	UFC	UFS	SFC	SNSNSN	UNUNUN
-ve	0.043	0.011	0.075	0.10	0.08	0	0	0.006
+ve	0.011	0.043	0.010	0.075	0	0.08	0.006	0

TABLE 3. Volume of available region for different topologies in p-q-r space (non-dimensional).

flow field- SNSS, UFC and SFS seem to last for more-or-less the same time showing not much sensitivity to either dilatation rate or Mach number.

To further understand the behavior observed in figure 11, we investigate two prospective reasons which may influence the lifetime of a topology of a fluid particle as it moves in the $p-q-r$ space: (i) the actual volume available to a topology in the $p-q-r$ space, and (ii) the velocity of the fluid particles in the $p-q-r$ space. The velocity of a particle in the $p-q-r$ space can be defined as the rate at which its three invariants, p, q and r, change with time. This rate is quantitifed as a velocity vector in the $p-q-r$ space. We denote this velocity vector by $\vec{U}_{pqr}$:

$$\vec{U}_{pqr} = \frac{dp}{dt}\hat{p} + \frac{dq}{dt}\hat{q} + \frac{dr}{dt}\hat{r}; \tag{5.9}$$

where $\frac{dp}{dt}$, $\frac{dq}{dt}$, and $\frac{dr}{dt}$ are rates of change of invariants following a fluid particle in accordance with (5.6). The symbols $\hat{p}$, $\hat{q}$ and $\hat{r}$ denote the unit vectors along the three mutually perpendicular axes of p, q and r coordinates. The quantity $\vec{U}_{pqr}$ is indeed a measure of how fast the footprint of a fluid particle is changing in the $p-q-r$ space.

It is observed that a smaller volume available to a topology in the $p-q-r$ space will be a contributing factor towards decreasing the lifetime of a topology, because a particle even if moving slowly will tend to crossover to the territory of neighboring topology sooner. On the other hand, a high magnitude of $\vec{U}_{pqr}$ of a fluid particle in the $p-q-r$ space will tend to bring the particle closer to the bounding surfaces quickly and thus contributing in reducing the lifetime of the topology associated with that fluid particle.

In Table 3 we present the volumes associated with the six major topologies that exist in compressible turbulence in the space of the normalized invriants p,q and r. These volumes have been reported separately on the positive and the negative side of the p axis. In figure 12(a-f) we present the magnitudes of the mean value of $\vec{U}_{pqr}$ calculated by taking the average of $\vec{U}_{pqr}$ over subsets of the tagged particles belonging to different topologies and different dilatation bins. The results of simulation G has been used to obtain these plots.

5.1.1. *UNSS and SNSS*

Referring first to the UNSS and SNSS topologies, we examine if the volume measures available in Table 3 and the conditional mean values of $\vec{U}_{pqr}$ available in figure 12 can help us understand the variation of lifetimes reported in figure 11. In figure 12 we observe that mean value of the magnitude of $\vec{U}_{pqr}$ is higher at positive/negative dilatations than what it is at at zero dilatation. Moreover, if we compare only the high positive and high negative dilatations, mean velocity is somewhat more at negative dilatations. On the other hand, Table 3 shows that the available volume of UNSS topology on the negative side is less than what it is one the positive side. A higher mean velocity associated with a smaller volume on the $a_{ii} < 0$ side, allows a particle with initial UNSS topology to quickly cross over to the territory of the neighboring topologies making its lifetime low as observed in figure 11(a). At zero dilatation, the velocity drops significantly thus allowing the fluid element to stay inside the UNSS territory for a longer duration. At positive dilatations,

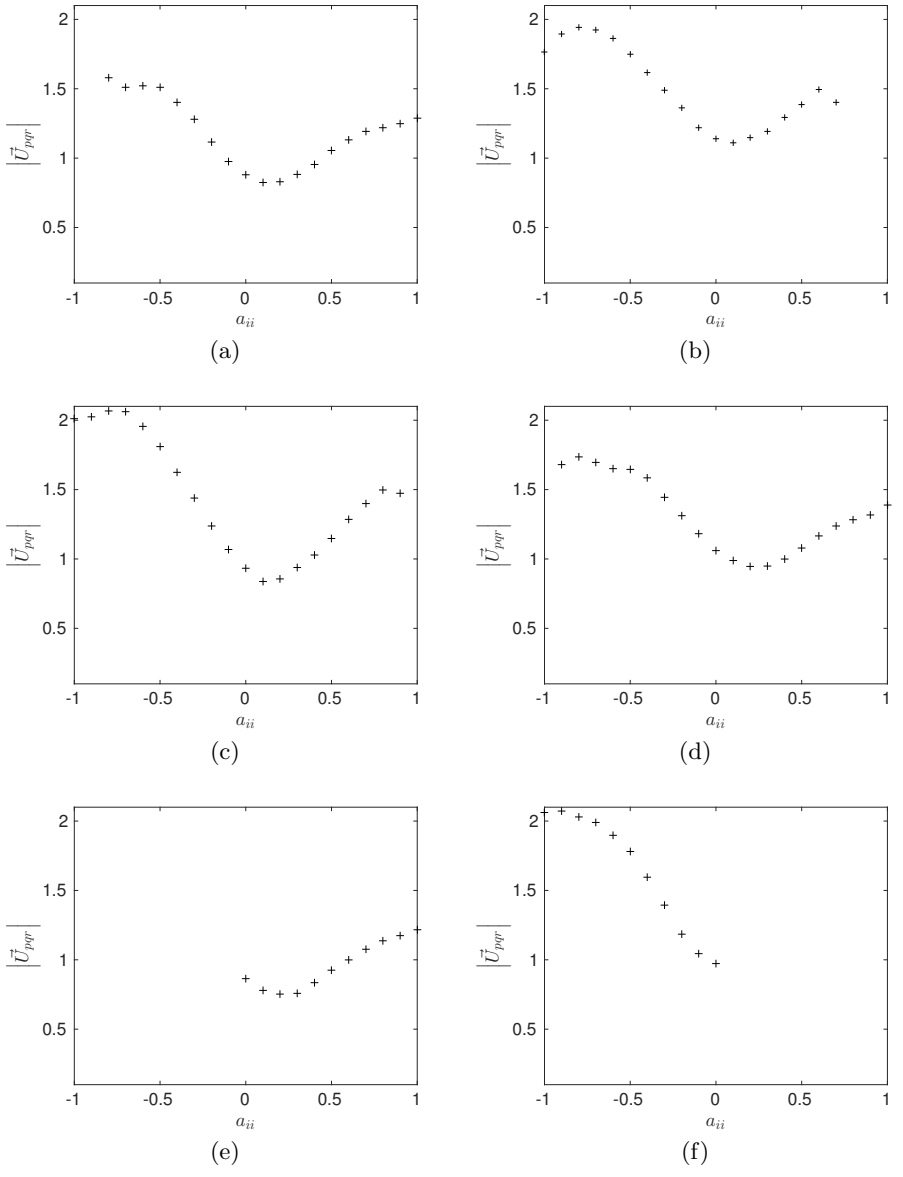

FIGURE 12. Variation of average velocity in p-q-r space $|U_{pqr}|$ with initial dilatation a_{ii} (bin size: $\overline{a_{ii}} \pm 0.05$) for 6 major topologies: (a)UNSS, (b)SNSS, (c)SFS, (d)UFC, (e)UFS and (f)SFC. (Simulation G)

even though the velocity is high, a significant increase in the volume of UNSS allows the lifetime to decrease moderately as evident in figure 11(a). In the case of SNSS topology, as dilatation increases from high negative dilatation to high positive dilatations, volume decreases. Velocity, however, deceases from a high value at negative to a very low value at zero dilatation (figure 12(b)). The drop in the available volume seems to be offset by a decrease in velocity keeping the average lifetime of topology more-or-less at the same level as it was at high negative dilatation. When dilatation increases to positive values, velocity increases (figure 12)−though not as much as it was at negative dilatations and

Simulation	UNSS	SNSS	SFS	UFC	UFS	SFC
A	0.23	0.28	0.23	0.26	-	-
E	0.88	1.37	0.97	1.03	0.87	1.46
G	1.01	1.57	1.13	1.18	0.90	1.76

TABLE 4. Average velocity of particles in p-q-r space ($|U_{pqr}| = |\frac{\partial p}{\partial t}\hat{p} + \frac{\partial q}{\partial t}\hat{q} + \frac{\partial r}{\partial t}\hat{r}|$) for various simulations (Table 1)

thus even a decrease in volume results into only a little increase in the lifetime (figure 11(b)).

Similar explanation can be provided for the variation in lifetimes observed in figure 11(c) and 11(d) for SFS and UFC topology using the volume data and mean magnitude of $\vec{U}_{pqr}$ of these topologies in figure 12(c) and 12(d).

For the UFS and SFC topologies we do not observe any change in lifetimes in figure 11(e). While UFS exists only at positive dilatation, SFC exists only at negative dilatations. For both these topologies the volumes increase as the magnitude of dilatation increases. Further, figure 11(e) clearly shows that their velocities also increase as the magnitude of normalized dilatation increases. For both these topologies, the increase in volume (which favors high lifetime) seem to be effectively counteracted by increase in mean velocity (which favors low lifetime) resulting into an almost dilatation-independent lifetime as evident in figure 11.

5.1.2. *Role of Mach number*

As observed earlier, in general, the influence of increasing initial turbulent Mach number is to decrease the lifetime of topologies (figure 11). The explanation of this trend is provided by Table 4, wherein we have included the mean magnitude of $\vec{U}_{pqr}$ in simulations A, E and G at $t_{ref} = 4.0\tau$. We observe that in general, an increase in initial turbulent Mach number increases mean velocity in the $p - q - r$ space, consequently reducing $\langle L_{\mathcal{T}} \rangle$ as evident in figure 11.

5.1.3. *Role of Reynolds number*

In figure 11 we have also shown results from simulation C-E. These simulations (C-E) have identical M_t and different Re_λ: 70, 100 and 150 respectively. We observe that the lifetimes recorded for all these similations are almost similar. Thus we conclude that, Reynolds number has negligible influence on the lifetime of topology.

Overall, our results in figure 11 clearly show that in terms of longevity, the six major topologies existing in compressible turbulence (Simulation G) can be arranged in the following descending order: SFS>UNSS>UFC>SNSS>UFS>SFC. Accordingly, it is plausible to expect that at a typical instant of this simulation, compressible decaying turbulence should have the highest population of particles associated with the SFS topology, lowest with the SFC topology and the populations of other four topologies falling in the same order as the order of their lifetimes. In Table 5 we present the population percentage of each of the six topologies at $t = 4\tau$ in Simulation G. We observe that indeed the percentage population of the six topologies decrease exactly in the same order as the order shown by them in terms of lifetimes. While previous studies have also reported the percentage population of various topologies in compressible turbulence

UNSS	SNSS	SFS	UFC	UFS	SFC
26.07	10.10	27.44	21.16	10.49	4.32

TABLE 5. Percentage topology composition for compressible simulation case G.

	UNSS	SNSS	SFS	UFC
Composition %	25.2	5.4	43.5	25.9
Lifetime (κ_τ)	1.80	0.53	3.32	2.08
Percentage % of time spent in different topologies CMTs Martín *et al.* (1998)	53	21.5	20	5.5

TABLE 6. Comparison of the performances of CMTs versus the approach adopted in this work. The composition and the computed lifetime (data in the first two rows) are from Simulation A of this work.

(Table 5) in other contexts (Suman & Girimaji 2010), the analysis presented in this work has provided a clear explanation of the same based on careful particle tracking and calculations of invariant dynamics using actual Lagrangian trajectories.

5.2. *CMT versus LT*

As mentioned in the Introduction, many researchers have adopted an alternate though approximate procedure of examining trajectories in the p-q-r space. This alternative method does not track the individual fluid particles at different time instants, but uses the averaged value of the rhs of (5.6) conditioned on a chosen set of p, q, r merely at one single time instant. The statistics thus obtained are essentially the conditional averages of the rate of change of the invariants with the conditional parameters being the local values of p, q, r. The trajectories thus obtained are the instantaneous streamlines in p-q-r space. Such trajectories are referred to as the conditional mean trajectories (CMT) (Martín *et al.* 1998). CMTs are approximate, and their use in the past studies can only be justified as a surrogate tool in the absence of adequate computational resources (Martín *et al.* 1998).

To further underline the significance of our present work using Lagrangian trajectories, we present Table 6, wherein we have included mean values of the lifetime of UNSS, SNSS, SFS and UFC topologies computed using flow fields of Simulation A. Note that Simulation A has very low initial Mach number and can be treated practically as an incompressible flow.

The percentage composition in terms of the four topologies in this flow field is included in Table 6 (at $t = 4\tau$). We observe that the mean lifetimes calculated using our Lagrangian approach for these four topologies are in almost the same proportion as the percentage population of the topologies. In the last row of Table 6 we have included the percentage of "time spent in various topologies" as calculated by Martín *et al.* (1998) using their CMT approach. Since Martín *et al.* (1998)'s CMTs do show a cyclic change in topology ($UFC \rightarrow UNSS \rightarrow SNSS \rightarrow SFS \rightarrow UFC$), the "time spent in various topologies" can be interpreted as the CMT-based estimate of lifetime of topologies. We find that the proportion of lifetimes calculated using CMTs are in gross disagreement with the percentage composition of incompressible turbulence.

To elucidate why CMTs fail significantly in capturing topology lifetimes (and probably other time dependents aspects of the dynamics of velocity gradients) we present a simple

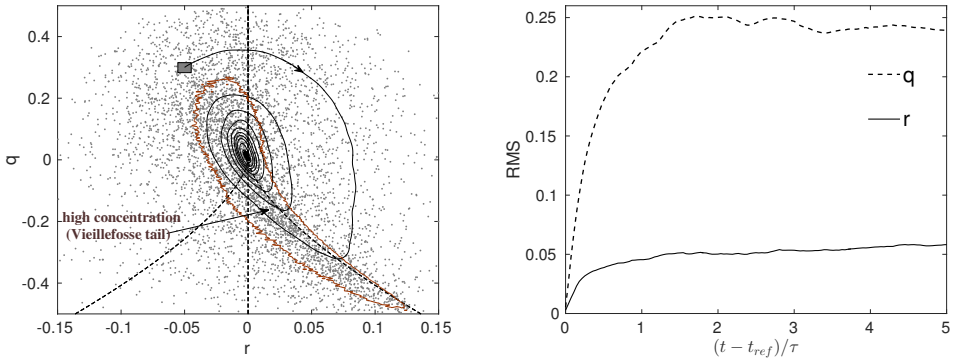

(a) (b)

FIGURE 13. (a) Evolution of root mean squared value of invariants q and r starting from a bounded region r (-0.05 ± 0.01) and q (0.3 ± 0.025) (b) Instantaneous CMT (solid line) and final spread of Lagrangian particles after 1 eddy-turnover time starting from the bounded region. Sample size of conditioned particles in the bounded region ≈ 5000.

comparison. In figure 13(a) we show a conditional mean trajectory (solid line) originating at point $(q = 0.3, r = -0.05)$. This CMT has been generated using one-time Eulerian field from Simulation A at $\tau = 4$ eddy-turnover time. The CMT shows a spiraling path around the origin. Performing a procedure of line integrations along such trajectories, Martín *et al.* (1998) estimate the characteristic "cycle time" of topology interconversion as three eddy turnover time. Next, we tag the same particles (in total 5,000) which were having their initial invariants in the vicinity of the $(q = 0.3, r = -0.05)$ at the reference time of four eddy-turnover time and track their movement on the $q - r$ plane. The locations of these 5,000 particles after just one eddy turnover time has been shown in figure 13(a) itself. It can be observed that the tagged population of particles spreads vastly over the q-r plane. Indeed the spread of this population sample is identical to the characteristic global distribution of particles of the entire flow field. This characteristic distribution has a tear-drop shape with the bulk of data concentrated on one side in the SFC region and on the other side along the curve separating the UFC and UNSS regions (the so-called vieillefosse tail, Vieillefosse (1982)). Further, in figure 13(b), we present the root mean squared value of q and r of the same sample of 5,000 particles which had their q, r in the vicinity of $(q = 0.3, r = -0.05)$ at the reference time of four eddy turnover time. The rms values start increasing and within just eddy-turnover time reach thier asymptotic states. The rms of q reaches an asymptotic state of 0.24, and the rms of r reaches an asymptotic state of 0.05. Indeed, these values match with the unconditioned rms values of q and r of all the particles that are present in the flow field. Thus, even one eddy turnover time is long enough a duration for particles to completely forget their initial association with a particular point in the q-r plane. Thus, employing CMTs to estimate phenomena which happen over this time scale is indeed not appropriate.

6. Conclusions

We investigate dynamics of velocity gradients in compressible decaying turbulence employing the Lagrangian approach of following a set of identified fluid particles. Well resolved direct numerical simulations over a wide range of turbulent Mach number and Reynolds number along with a well validated Lagrangian particle tracker are employed for this study. In the first part of our work, we focus on the viscous diffusion process

incumbent in the exact evolution equation of the velocity gradient tensor. Specifically, we investigate the influence of Mach number on this process. We find that the initial turbulent Mach number has considerable influence on the Lagrangian statistics of the viscous process. We provide evidence and explain that this intensification is attributable to the development of a large disparity in the magnitude of the velocity gradients associated with contracting and expanding fluid particles combined with the overall preferences of these contracting and expanding fluid particles to change their dilatation rate (Section 4.1). Our investigation of the exact process is followed up by evaluation of the so called Linear Lagrangian Diffusion model (LLDM) of the viscous process (section 4.2). Using Lagrangian tracking we clearly demonstrate that the LLD model shows an unphysical exponential behavior which is in gross disagreement with the exact Lagrangian evolution of the viscous process seen in DNS, especially in the late stages of the turbulence decay. We argue that the unrealistic behavior of the LLD model is attributable to the assumption that the fourth order tensor representing the Lagrangian Hessian of the velocity gradient tensor remains isotropic at all times. Finally, we propose a possible modeling approach with which this shortcoming can eb addressed.

In the second part of the study we examine the dynamics of the invariants of the velocity gradient tensor using the Lagrangian approach and compute lifetimes of various topologies in compressible turbulence. In particular, we identify the role of initial turbulent Mach number and the normalized dilatation rate on topology lifetimes. Explanation of the identified trends are then provided in terms of the geometric constraint of the $p-q-r$ space and the disparity in the speed of the fluid particles in the $p-q-r$ space. Further, using our Lagrangian data and analysis we clearly demonstrate the limitation of the so-called conditional mean trajectory (CMT) in explaining certain aspects of the dynamics of velocity gradient invariants.

7. Acknowledgments

The authors acknowledge the computational support provided by the High-Performance Computing Center (HPC) of the Indian Institute of Technology Delhi, India.

REFERENCES

Ashurst, Wm. T., Chen, J-Y & Rogers, M. M. 1987*a* Pressure gradient alignment with strain rate and scalar gradient in simulated Navier–Stokes turbulence. *Phys. Fluids* **30** (10), 3293–3294.

Ashurst, Wm. T., Kerstein, A. R., Kerr, R. M. & Gibson, C. H. 1987*b* Alignment of vorticity and scalar gradient with strain rate in simulated Navier–Stokes turbulence. *Phys. Fluids* **30** (8), 2343–2353.

Atkinson, Callum, Chumakov, Sergei, Bermejo-Moreno, Ivan & Soria, Julio 2012 Lagrangian evolution of the invariants of the velocity gradient tensor in a turbulent boundary layer. *Phys. Fluids* **24** (10), 105104.

Bechlars, P. & Sandberg, R. D. 2017 Evolution of the velocity gradient tensor invariant dynamics in a turbulent boundary layer. *J. Fluid Mech.* **815**, 223242.

Bhatnagar, Akshay, Gupta, Anupam, Mitra, Dhrubaditya, Pandit, Rahul & Perlekar, Prasad 2016 How long do particles spend in vortical regions in turbulent flows? *Phys. Rev. E* **94** (5), 1–8.

Cantwell, Brian & Coles, Donald 1983 An experimental study of entrainment and transport in the turbulent near wake of a circular cylinder. *Journal of fluid mechanics* **136**, 321–374.

Cantwell, Brian J. 1992 Exact solution of a restricted Euler equation for the velocity gradient tensor. *Phys. Fluids A* **4** (4), 782–793.

Cantwell, Brian J. 1993 On the behavior of velocity gradient tensor invariants in direct numerical simulations of turbulence. *Phys. Fluids A* **5** (8), 2008–2013.

Chen, Hudong, Herring, Jackson R., Kerr, Robert M. & Kraichnan, Robert H. 1989 Non-Gaussian statistics in isotropic turbulence. *Phys. Fluids A* **1** (11), 1844–1854.

Chevillard, Laurent & Meneveau, Charles 2006 Lagrangian dynamics and statistical geometric structure of turbulence. *Phys. Rev. Lett.* **97** (17), 174501.

Chevillard, Laurent & Meneveau, Charles 2011 Lagrangian time correlations of vorticity alignments in isotropic turbulence: Observations and model predictions. *Phys. Fluids* **23** (10), 101704.

Chevillard, Laurent, Roux, SG, Lévêque, Emmanuel, Mordant, Nicolas, Pinton, J-F & Arnéodo, Alain 2003 Lagrangian velocity statistics in turbulent flows: Effects of dissipation. *Phys. Rev. Lett.* **91** (21), 214502.

Chong, M. S., Perry, A. E. & Cantwell, B. J. 1990 A general classification of three-dimensional flow fields. *Phys. Fluids A* **2** (5), 765–777.

Chu, You-Biao & Lu, Xi-Yun 2013 Topological evolution in compressible turbulent boundary layers. *J. Fluid Mech.* **733**, 414–438.

Danish, Mohammad, Sinha, Sawan Suman & Srinivasan, Balaji 2016*a* Influence of compressibility on the lagrangian statistics of vorticity–strain-rate interactions. *Phys. Rev. E* **94** (1), 013101.

Danish, Mohammad, Suman, Sawan & Girimaji, Sharath S 2016*b* Influence of flow topology and dilatation on scalar mixing in compressible turbulence. *J. Fluid Mech.* **793**, 633–655.

Danish, Mohammad, Suman, Sawan & Srinivasan, Balaji 2014 A direct numerical simulation-based investigation and modeling of pressure Hessian effects on compressible velocity gradient dynamics. *Phys. Fluids* **26** (12), 126103.

Elghobashi, S. & Truesdell, G. C. 1992 Direct simulation of particle dispersion in a decaying isotropic turbulence. *J. Fluid Mech.* **242**, 655700.

Elsinga, G. E. & Marusic, I. 2010 Evolution and lifetimes of flow topology in a turbulent boundary layer. *Physics of Fluids* **22** (1), 015102.

Girimaji, S.S. 1991 Assumed β-pdf Model for Turbulent Mixing: Validation and Extension to Multiple Scalar Mixing. *Combustion Science and Technology* **78** (4-6), 177–196.

Girimaji, S. S. & Pope, S. B. 1990*a* A diffusion model for velocity gradients in turbulence. *Phys. Fluids A* **2** (2), 242–256.

Girimaji, S. S. & Pope, S. B. 1990*b* Material-element deformation in isotropic turbulence. *J. Fluid Mech.* **220**, 427–458.

Girimaji, Sharath S. & Speziale, Charles G. 1995 A modified restricted Euler equation for turbulent flows with mean velocity gradients. *Phys. Fluids* **7** (6), 1438–1446.

Jeong, Eunhwan & Girimaji, Sharath S. 2003 Velocity-gradient dynamics in turbulence: Effect of viscosity and forcing. *Theor. Comp. Fluid Dyn.* **16** (6), 421–432.

Kerimo, Johannes & Girimaji, Sharath S. 2007 Boltzmann–BGK approach to simulating weakly compressible 3D turbulence: comparison between lattice Boltzmann and gas kinetic methods. *J. Turbul.* **8** (46), 1–16.

Kumar, G., Girimaji, Sharath S. & Kerimo, J. 2013 WENO-enhanced gas-kinetic scheme for direct simulations of compressible transition and turbulence. *J. Comput. Phys.* **234**, 499–523.

Lee, Kurnchul, Girimaji, Sharath S. & Kerimo, Johannes 2009 Effect of compressibility on turbulent velocity gradients and small-scale structure. *J. Turbul.* **10** (9), 1–18.

Liao, Wei, Peng, Yan & Luo, Li-Shi 2009 Gas-kinetic schemes for direct numerical simulations of compressible homogeneous turbulence. *Phys. Rev. E* **80** (4), 046702.

Lüthi, Beat, Tsinober, Arkady & Kinzelbach, Wolfgang 2005 Lagrangian measurement of vorticity dynamics in turbulent flow. *J. Fluid Mech.* **528**, 87–118.

Martín, Jesús, Ooi, Andrew, Chong, M.S. & Soria, Julio 1998 Dynamics of the velocity gradient tensor invariants in isotropic turbulence. *Phys. Fluids* **10**, 2336–2346.

Martín, M Pino, Taylor, Ellen M, Wu, Minwei & Weirs, V Gregory 2006 A bandwidth-optimized WENO scheme for the effective direct numerical simulation of compressible turbulence. *J. Comput. Phys.* **220** (1), 270–289.

Meneveau, Charles 2011 Lagrangian dynamics and models of the velocity gradient tensor in turbulent flows. *Annu. Rev. Fluid Mech.* **43**, 219–245.

Ohkitani, Koji 1993 Eigenvalue problems in three-dimensional Euler flows. *Phys. Fluids A* **5** (10), 2570–2572.

O'Neill, Philippa & Soria, Julio 2005 The relationship between the topological structures in turbulent flow and the distribution of a passive scalar with an imposed mean gradient. *Fluid Dyn. Res.* **36** (3), 107–120.

Ooi, Andrew, Martin, Jesus, Soria, Julio & Chong, M.S. 1999 A study of the evolution and characteristics of the invariants of the velocity-gradient tensor in isotropic turbulence. *J. Fluid Mech.* **381**, 141–174.

Parashar, N., Sinha, S. S., Danish, M. & Srinivasan, B. 2017*a* Lagrangian investigations of vorticity dynamics in compressible turbulence. *Physics of Fluids* **29** (10), 105110.

Parashar, N., Sinha, S. S., Srinivasan, B. & Manish, A. 2017*b* Gpu-accelerated direct numerical simulations of decaying compressible turbulence employing a gkm-based solver. *Int. J. Numer. Meth. Fluids* **83** (10), 737–754.

Pirozzoli, S. & Grasso, F. 2004 Direct numerical simulations of isotropic compressible turbulence: influence of compressibility on dynamics and structures. *Phys. Fluids* **16** (12), 4386–4407.

Pope, Stephen B. 2002 Stochastic Lagrangian models of velocity in homogeneous turbulent shear flow. *Phys. Fluids* **14** (5), 1696–1702.

Pumir, Alain 1994 A numerical study of the mixing of a passive scalar in three dimensions in the presence of a mean gradient. *Phys. Fluids* **6** (6), 2118–2132.

Samtaney, Ravi, Pullin, Dale I. & Kosovic, Branko 2001 Direct numerical simulation of decaying compressible turbulence and shocklet statistics. *Phys. Fluids* **13** (5), 1415–1430.

da Silva, Carlos B. & Pereira, José C.F. 2008 Invariants of the velocity-gradient, rate-of-strain, and rate-of-rotation tensors across the turbulent/nonturbulent interface in jets. *Phys. Fluids* **20** (5), 55101–55101.

Soria, J., Sondergaard, R., Cantwell, B. J., Chong, M. S. & Perry, A. E. 1994 A study of the fine-scale motions of incompressible time-developing mixing layers. *Phys. Fluids* **6** (2), 871–884.

Suman, S. & Girimaji, S. S. 2009 Homogenized Euler equation: a model for compressible velocity gradient dynamics. *J. Fluid Mech.* **620**, 177–194.

Suman, Sawan & Girimaji, Sharath S. 2010 Velocity gradient invariants and local flow-field topology in compressible turbulence. *J. Turbul.* **11** (2), 1–24.

Suman, Sawan & Girimaji, Sharath S. 2012 Velocity-gradient dynamics in compressible turbulence: influence of Mach number and dilatation rate. *J. Turbul.* **13** (8), 1–23.

Vaghefi, Navid S. & Madnia, Cyrus K. 2015 Local flow topology and velocity gradient invariants in compressible turbulent mixing layer. *J. Fluid Mech.* **774**.

Vieillefosse, P. 1982 Local interaction between vorticity and shear in a perfect incompressible fluid. *J. Phys.* **43** (6), 837–842.

Wang, Li & Lu, Xi-Yun 2012 Flow topology in compressible turbulent boundary layer. *J. Fluid Mech.* **703**, 255–278.

Xu, Haitao, Pumir, Alain & Bodenschatz, Eberhard 2011 The pirouette effect in turbulent flows. *Nature Phys.* **7** (9), 709–712.

Xu, Kun 2001 A gas-kinetic BGK scheme for the Navier–Stokes equations and its connection with artificial dissipation and Godunov method. *J. Comput. Phys.* **171** (1), 289–335.

Yeung, P. K. & Pope, S. B. 1988 An algorithm for tracking fluid particles in numerical simulations of homogeneous turbulence. *J. Comput. Phys.* **79** (2), 373–416.

Yeung, P. K. & Pope, S. B. 1989 Lagrangian statistics from direct numerical simulations of isotropic turbulence. *J. Fluid Mech.* **207**, 531–586.

Zhou, Yi, Nagata, Koji, Sakai, Yasuhiko, Ito, Yasumasa & Hayase, Toshiyuki 2015 On the evolution of the invariants of the velocity gradient tensor in single-square-grid-generated turbulence. *Physics of Fluids* **27** (7), 075107.